

UCSF

UC San Francisco Previously Published Works

Title

Denosing of hyperpolarized ¹³C MR images of the human brain using patch-based higher-order singular value decomposition

Permalink

<https://escholarship.org/uc/item/9jv233xw>

Journal

Magnetic Resonance in Medicine, 86(5)

ISSN

0740-3194

Authors

Kim, Yaewon

Chen, Hsin-Yu

Autry, Adam W

et al.

Publication Date

2021-11-01

DOI

10.1002/mrm.28887

Peer reviewed



Published in final edited form as:

Magn Reson Med. 2021 November ; 86(5): 2497–2511. doi:10.1002/mrm.28887.

Denoising of Hyperpolarized ^{13}C MR Images of the Human Brain Using Patch-based Higher-order Singular Value Decomposition

Yaewon Kim¹, Hsin-Yu Chen¹, Adam W. Autry¹, Javier Villanueva-Meyer¹, Susan M. Chang², Yan Li¹, Peder E. Z. Larson¹, Jeffrey R. Brender³, Murali C. Krishna³, Duan Xu¹, Daniel B. Vigneron^{1,2}, Jeremy W. Gordon^{1,*}

¹Department of Radiology and Biomedical Imaging, University of California, San Francisco, CA, USA.

²Department of Neurological Surgery, University of California, San Francisco, CA, USA.

³Center for Cancer Research, National Cancer Institute, National Institutes of Health, Bethesda, MD, USA.

Abstract

Purpose—To improve hyperpolarized ^{13}C (HP- ^{13}C) MRI by image denoising with a new approach, patch-based higher-order singular value decomposition (HOSVD).

Methods—The benefit of using a patch-based HOSVD method to denoise dynamic HP- ^{13}C MR imaging data was investigated. Image quality and the accuracy of quantitative analyses following denoising were evaluated first using simulated data of [1- ^{13}C]pyruvate and its metabolic product, [1- ^{13}C]lactate, and compared the results to a global HOSVD method. The patch-based HOSVD method was then applied to healthy volunteer HP [1- ^{13}C]pyruvate echo-planar imaging (EPI) studies. Voxel-wise kinetic modeling was performed on both non-denoised and denoised data to compare the number of voxels quantifiable based on SNR criteria and fitting error.

Results—Simulation results demonstrated an 8-fold increase in the calculated signal-to-noise ratio (SNR) of [1- ^{13}C]pyruvate and [1- ^{13}C]lactate with the patch-based HOSVD denoising. The voxel-wise quantification of k_{PL} (pyruvate-to-lactate conversion rate) showed a 9-fold decrease in standard errors for the fitted k_{PL} after denoising. The patch-based denoising performed superior to the global denoising in recovering k_{PL} information. In volunteer datasets, [1- ^{13}C]lactate and [^{13}C]bicarbonate signals became distinguishable from noise across captured timepoints with over a 5-fold apparent SNR gain. This resulted in >3-fold increase in the number of voxels quantifiable for mapping k_{PB} (pyruvate-to-bicarbonate conversion rate) and whole brain coverage for mapping k_{PL} .

Conclusions—Sensitivity enhancement provided by this denoising significantly improved quantification of metabolite dynamics and could benefit future studies by improving image quality,

*Correspondence: Jeremy W. Gordon, Department of Radiology and Biomedical Imaging, University of California San Francisco, 1700 4th St, Byers Hall 102, San Francisco, CA 94158, USA. Jeremy.Gordon@ucsf.edu.

Data Availability Statement

The code and data that support the findings of this study are openly available in hp13C_EPI-hosvd_denoising at https://github.com/ykim-hmtrc/hp13c_EPI-hosvd_denoising.

enabling higher spatial resolution, and facilitating the extraction of metabolic information for clinical research.

Keywords

hyperpolarized C-13 pyruvate; image denoising; higher-order singular value decomposition

1. Introduction

Hyperpolarization (HP) of ^{13}C nuclei via dynamic nuclear polarization provides a significant MR signal enhancement of 4 to 5 orders of magnitude,¹ which has enabled non-invasive measurements of real-time energy metabolism of hyperpolarized substrates and downstream metabolites.^{2,3} Various HP metabolic precursors, including carbon-13 enriched pyruvate,^{4,5} glucose,⁶ α -ketoglutarate⁷ and others,⁸ have been shown to serve as probes for assessing different metabolic pathways in the brain that would otherwise be difficult to access. Among those precursors, HP- ^{13}C pyruvate is the only probe translated into clinical use to date.^{9,10} In clinical research of multiple brain tumors, HP [1- ^{13}C]pyruvate has been used to report on the upregulated glycolytic metabolism of [1- ^{13}C]pyruvate-to-[^{13}C]lactate conversion in lesions (Warburg effect),^{11,12} measure [^{13}C]bicarbonate production^{13–15}, and assess metabolic changes induced by treatment response.¹⁶ Recent studies in healthy volunteers have also shown region-specific and age-dependent lactate production in the brain using HP [1- ^{13}C]pyruvate.^{17,18}

Despite the enormous gain in MR signal by hyperpolarization as well as its capability of accessing multiple metabolic pathways, a limitation of this method comes from the non-renewable decay of hyperpolarization via spin-lattice nuclear spin relaxation (T_1). Typically, T_1 relaxation of ^{13}C spins is on the order of several tens of seconds, which limits the temporal window for acquiring HP signals to approximately 1 – 2 min. This limits the monitoring of the kinetics of conversions to downstream metabolites such as [^{13}C]bicarbonate when using HP [1- ^{13}C]pyruvate due to slow pyruvate-to-bicarbonate conversion and short T_1 of bicarbonate. To tackle this problem, various fast acquisition strategies have been developed to efficiently utilize HP signals in the limited time available including specialized pulse sequences^{19–22} such as variable flip angle schemes²³ and variable resolution imaging approaches²⁴ as well as hardware improvements such as parallel imaging using multi-channel receive arrays for ^{13}C imaging.^{25,26}

Image denoising also can improve HP- ^{13}C MR image quality following data acquisition. Multiple algorithms have been proposed to denoise multiparametric MRI data. These methods can be roughly divided into two groups. The first treats the dataset as a stack of images and denoises each one individually, generally assuming a similarity between neighboring voxels (non-local means and patch-based methods)^{27–29} or by truncating a succession of increasingly accurate approximations to the image (wavelet and low-rank methods).^{30–33} The second assumes a similarity between the same spatial image acquired at different time points or with different parameters (T_1 -, T_2 -, CEST, and diffusion imaging).^{34,35} These methods generally employ higher-order singular value decomposition (HOSVD), which is a generalization of matrix SVD for higher dimensions,^{36,37} to globally

approximate the multidimensional dataset in terms of a combination of lower dimensional features. The HOSVD technique is particularly powerful when applied to dynamic MR spectral data, as the spatial variance in the signal is typically much higher than the spectral variance (chemical shifts do not change greatly with time or throughout the image). Using this technique, it was possible to improve quantification of low-SNR metabolites that were otherwise undetectable in both preclinical³⁸ and clinical conditions.³⁹

For HP MRI, the two methods can be combined by performing the HOSVD at the patch level by taking into account similarity within patches in nearby regions in the image.³⁷ By applying the HOSVD transform to a group of similar local patches, the similarity within the group, in addition to all dimensions of multidimensional data, can be exploited for effective noise removal. This patch-based HOSVD method showed superior performance over the global HOSVD when applied to diffusion-weighted ¹H MR images.³⁵ However, HP-¹³C EPI images are acquired at lower resolution than conventional MRI (typically 16×16 versus 128×128 and higher), and it was uncertain if a patch-based method would be effective. In this study, we compared the denoising performance of global and patch-based HOSVD methods using simulated dynamic ¹³C metabolic data, and then investigated patch-based HOSVD denoising in healthy volunteer brain HP-¹³C EPI data acquired using multichannel arrays and a single channel quadrature head coil.

2. Methods

2.1 HOSVD-based denoising for dynamic HP-¹³C MR images

2.1.1 Patch-based HOSVD denoising method—The patch-based HOSVD denoising method implemented in this study was adapted from the global-local HOSVD (GL-HOSVD) denoising algorithm demonstrated on diffusion-weighted ¹H MRI data by Zhang et al.³⁴ Figure 1 illustrates the GL-HOSVD algorithm for denoising dynamic HP-¹³C EPI data. It consists of two main stages. The first stage involves prefiltering noisy images by applying the HOSVD transform globally to the whole dynamic data, which was shown to alleviate stripe-like artifacts in denoised images with low SNR that occur when pure patch-based HOSVD was used. For multi-slice acquisitions, each slice of the dynamic HP-¹³C MR imaging data comprises two spatial (x and y) and one temporal dimension, which can be represented as a 3D tensor. The HOSVD transform for this 3D tensor of size ($d_1 \times d_2 \times d_3$), defined as I , can be written as

$$I = \left[S; U^{(1)}, U^{(2)}, U^{(3)} \right] = S \times_1 U^{(1)} \times_2 U^{(2)} \times_3 U^{(3)} \quad (\text{Eq. 1})$$

where S is the core tensor of size ($d_1 \times d_2 \times d_3$) consisting of transform coefficients; $U^{(k)}$ ($k = 1, 2, 3$) is a factor matrix of size ($d_k \times d_k$) for the k^{th} dimension; and \times_k is a mode- k product of the tensor I by a matrix $U^{(k)}$.³⁶ The S and $U^{(k)}$ are first computed by performing SVD to the mode- k unfolding of the tensor I . The pre-filtered images are then obtained by using hard thresholding of the core tensor comprised of small transform coefficients contributing noise to the data. This threshold is determined based on the noise level of the original data and the size of tensor, scaled by a parameter k_{global} to effectively suppress the noise.⁴⁰ The pre-filtered images are reconstructed by the inverse HOSVD transform. In the

second stage, the local HOSVD begins by grouping similar 3D patches in the pre-filtered images into stacks. The similar patches are searched in a search window of size $(N_{sw} \times N_{sw})$ based on the sum of squared differences between the intensities of two input patches, one of which is a reference. Next, the selected patches are arranged into a 4D tensor (G_p) based on the similarity to the reference patch. The tensor G_p is then decomposed into the core tensor S_p and four factor matrices $U_p^{(k)}$ ($k = 1, 2, 3, 4$), as expressed by

$$G_p = [S_p; U_p^{(1)}, U_p^{(2)}, U_p^{(3)}, U_p^{(4)}] \quad (\text{Eq. 2})$$

Similarly, G_n is constructed from the original data using the patches at the same coordinates as those selected from the pre-filtered data. Subsequently, the core tensor S_n for the original data is reconstructed using the factor matrices U_p :

$$S_n = [G_n; U_p^{(1)T}, U_p^{(2)T}, U_p^{(3)T}, U_p^{(4)T}] \quad (\text{Eq. 3})$$

Through a hard-threshold operation on the transform coefficients in S_n , a noise-suppressed core tensor \widehat{S}_n can be obtained. A scaling factor k_{local} is used to manipulate the statistically derived threshold for an effective noise removal at the patch level. The denoised tensor \widehat{G}_n can be estimated by performing.

$$\widehat{G}_n = [\widehat{S}_n; U_p^{(1)}, U_p^{(2)}, U_p^{(3)}, U_p^{(4)}] \quad (\text{Eq. 4})$$

This patch-wise denoising of G_p is carried out across the image domain by moving the search window with a step size of N_{step} . The final denoised images are then reconstructed by aggregating the multiple estimates at each pixel. The code for GL-HOSVD was modified based on existing scripts and is available online (<https://github.com/XinyuanZhang719/gl-hosvd>).

2.1.2 TRI Denoising Method—We used the TRI (Tensor Rank truncation-Image enhancement) method³⁹ to denoise metabolite images in the simulations for a comparison of the denoising performance to the GL-HOSVD. The TRI method applies the HOSVD transform (Eq. 1) to the entire data series as in the first stage of GL-HOSVD. Regardless of the global or patch-based approach to denoising, the major difference between the two algorithms lies in how small transform coefficients are removed via manipulation of the tensor core. The TRI method employs a low-rank approximation (fixed number of non-zero values in S_n) while the GL-HOSVD method utilizes hard thresholding to eliminate small values in the core tensor S_n . In practical terms, this means GL-HOSVD can be parameterized directly from the noise level of the image while TRI requires prior knowledge or extensive simulations to estimate the rank.

2.2 Simulations

2.2.1. Designing a simulation framework—A brain phantom was created using gray and white matter extracted from a normal brain model accessible from the BrainWeb Simulated Brain Database.⁴¹ The matrix size ($N_x \times N_y$) was 32×32 (spatial resolution of $6.8 \times 6.8 \text{ mm}^2$) and was chosen to provide sufficient structural detail in the simulated

^{13}C MR dataset. Dynamic signals of pyruvate and lactate in the brain phantom were simulated using an irreversible, two-site kinetic model utilizing the hyperpolarized-mri-toolbox from GitHub (<https://github.com/LarsonLab/hyperpolarized-mri-toolbox/>).⁴² The rate of pyruvate-to-lactate conversion (k_{PL}) for gray and white matter was respectively set to 0.015 and 0.0075 s^{-1} , similar to the k_{PL} values observed from our own data^{16,43} and those reported by Grist et al.¹⁸ The T_1 relaxation times for $[1-^{13}\text{C}]$ pyruvate and $[1-^{13}\text{C}]$ lactate were set as 30 s and 25 s, respectively, in simulations. Other input parameters included flip angles $\alpha_{\text{pyruvate}}/\alpha_{\text{lactate}} = 20^\circ/30^\circ$, 3 s TR and 20 timeframes (N_t). This kinetic modeling utilized the measured pyruvate signals as the input at each timepoint and accounted for the signal loss via T_1 relaxation and RF pulses. The maximum intensity of the dynamic lactate signals was normalized to 1. To vary the SNR in the simulated datasets, zero-mean random Gaussian noise of $\sigma_n = 0.2, 0.3$ and 0.4 was added to the noise-free dynamic images of pyruvate and lactate, resulting in peak dynamic SNR of 14.6 to 29.2 for pyruvate and 2.5 to 5 for lactate. At the highest noise level ($\sigma_n = 0.4$), the peak signal intensity of lactate was within $3\sigma_n$ of the mean of noise distribution. This SNR range is close to or lower than that of in-vivo data acquired in our study. Using the noise-added image sets, the parameters for GL-HOSVD and TRI were determined empirically from simulation based on the root-mean-square error (RMSE) between the ground truth and denoised images and the SNR gain. The five GL-HOSVD parameters were the patch size $p \times p$ of 5×5 ; search window size N_{sw} of 11; step length N_{step} of 2; scales k_{global} of 0.4 and k_{local} of 0.8. For TRI, a tensor rank of (20, 20, 4) was chosen from a data matrix size (N_x, N_y, N_t) = (32, 32, 20). To avoid cross-contaminating signals between slices and metabolites, the denoising was performed independently on different slices of the brain images and also on different metabolites. For each denoising method, a total of 500 simulations were conducted per noise level, and k_{PL} values were determined voxel-by-voxel using the kinetic modeling designed to generate the metabolic phantom.

2.2.2 Assessment of denoising performance analysis—The sensitivity enhancement was evaluated by comparing the mean SNR of metabolic signals between denoised and non-denoised images. The image quality of the denoised data was assessed using structural similarity index metric (SSIM)⁴⁴ with respect to the noise-free data. A brain mask was applied to the images in order to exclude background voxels in the SSIM calculation. To assess the accuracy of k_{PL} quantification introduced by denoising, k_{PL} errors were calculated as $|true\ k_{\text{PL}} - estimated\ k_{\text{PL}}|/true\ k_{\text{PL}} \times 100$ (%), and k_{PL} precision was determined by the relative standard error calculated as $\sigma_{k_{\text{PL}}}/k_{\text{PL}} \times 100$ (%), where $\sigma_{k_{\text{PL}}}$ is a standard deviation obtained from non-linear least-square fitting of k_{PL} .

2.3 Brain studies in healthy volunteers

2.3.1 MR experiments—The HP- ^{13}C metabolic data of the brain ($N = 6$) in this study were acquired from two healthy volunteers using a 2D multi-slice EPI sequence,⁴⁵ following the injection of 250 mM HP $[1-^{13}\text{C}]$ pyruvate. The pulse sequence consisted of a single-band spectral-spatial RF pulse that sequentially excited $[1-^{13}\text{C}]$ pyruvate, $[1-^{13}\text{C}]$ lactate, and $[^{13}\text{C}]$ bicarbonate resonances with $20^\circ, 30^\circ, 30^\circ$ flip angles, respectively. Data were acquired with an in-plane spatial resolution of $1.5 \times 1.5\ \text{cm}^2$ ($24.0 \times 24.0\ \text{cm}^2$ FOV, 16×16 matrix) for 8 slices with 1.5 cm thickness, with 62.5 s TR, 21.7 ms TE, and 1.03

ms echo-spacing. Twenty timeframes were acquired per metabolite with a 3 s temporal resolution, yielding a total scan time of 60 s. Hyperpolarization of $[1-^{13}\text{C}]$ pyruvate was achieved by polarizing the samples for at least 2 hrs using a 5T SPINlab operating at 0.8 K (GE Healthcare, Chicago, IL). For anatomic reference, proton T_2 -weighted and 3D T_1 -weighted images were acquired. All experiments were performed on a 3T clinical MR scanner (MR750, GE Healthcare, Waukesha, WI) equipped with multi-nuclear imaging capability. For $\text{HP-}^{13}\text{C}$ MRI, either a 32-channel custom-built receiver (UCSF-MGH)²⁵ (datasets HV-01, HV-04) or a 24-channel receiver (Rapid Biomedical, Rimper, Germany) (datasets HV-02, HV-03, HV-05) were utilized in combination with birdcage RF transmit coils. A custom-built volume transmit/receive birdcage coil (UCSF-MGH) was used to obtain dataset HV-06 (see Table S1). Transmit RF power was calibrated on a head-shaped phantom containing unenriched ethylene glycol ($\text{HOCH}_2\text{CH}_2\text{OH}$, anhydrous, 99.8%, Sigma Aldrich, St. Louis, MO) prior to the volunteer study. All human studies were approved by an institutional review board requiring informed consent and followed Food and Drug Administration investigational new drug application (FDA IND)-approved protocols.

2.3.2 Data analysis—All EPI datasets were reconstructed using the Orchestra toolbox (GE Healthcare). First, phase coefficients from the reference scan were applied to the raw k-space data to correct for EPI Nyquist ghost artifacts. For multi-channel data, k-space data were pre-whitened and then coil-combined using estimated coil weights derived from the pyruvate data.⁴⁶ Complex data were phased to maximize the real part of the image, which was used for denoising and kinetic analysis, and retained the Gaussian noise distribution. To create brain masks for kinetic modeling, the T_1 -weighted images were first aligned by FLIRT⁴⁷ to the T_2 -fast spin echo images acquired prior to the ^{13}C examination, and then white/gray matter segmentation was performed on the aligned T_1 -weighted images using the FSL FAST algorithm.⁴⁸ The ^{13}C data voxels containing > 10% of white or gray matter were selected to generate whole brain masks, and kinetically modeled to obtain k_{PL} and k_{PB} maps. After fitting, only those voxels satisfying that the SNR_{auc} (SNR of temporally summed metabolic signals) is > 3 for pyruvate and lactate/bicarbonate in the raw data and that only voxels where $\sigma_{k_{\text{PX}}} < 0.3 \cdot k_{\text{PX}}$ ($X = \text{L or B}$) in the fit were included in the kinetic maps.⁴³ The SNR cutoff was determined from the k_{PL} error analysis in the numerical simulations to obtain reasonable kinetic rate maps. Other fit parameters include the T_1 relaxation time constants that were chosen to optimally fit the data. The number of voxels with k_{PL} or k_{PB} fulfilling the SNR and fitting error criteria were counted from the whole brain to calculate the spatial coverage in k_{PL} or k_{PB} maps. The total number of the ^{13}C data voxels was determined from the brain mask.

2.3.3 Simulations based on the experimental data—To investigate the performance of GL-HOSVD on experimental data with added noise, a total of 10 simulated pyruvate and lactate datasets were generated from one healthy volunteer dataset by deteriorating the data with zero-mean random Gaussian noise of $\sigma = 0.8, 1.2$ and 1.6 . With the additive noise, the noise level of the simulated datasets was 3, 4 and 5 times higher than that of the original data. From the noise-added and GL-HOSVD denoised images, k_{PL} was determined as described in the following sections. All data analysis and simulation work

(https://github.com/ykim-hmtrc/hp13c_EPI-hosvd_denoising) were performed in MATLAB R2019a (The MathWorks Inc., Natick, MA).

3. Results

3.1 Simulated denoising results

3.1.1 Image quality—In Figure 2A, the images in the first two columns show the simulated $[1-^{13}\text{C}]$ pyruvate and $[1-^{13}\text{C}]$ lactate ground truth (noise-free) images and those with additive 30% random Gaussian noise ($\sigma_n = 0.3$) from a central slice of the brain phantom at an early ($t = 12$ s) and later (36 s) timepoint. At this noise level, the peak dynamic SNR was respectively 19.5 and 3.3 for pyruvate and lactate. The images in the third column were produced by applying GL-HOSVD to the noise-added images. The gray and white matter is well separated in the denoised pyruvate images, where the signal intensities from the two compartments are similar. It is also apparent that the denoised lactate images, with signal intensities that are near the noise floor in the noise-added data, closely resemble the noise-free images. For comparison, the Tensor Rank truncation-Image enhancement (TRI) method was applied to reduce noise from the same noise-added images, and the resultant images are shown in the last column. This TRI method was previously demonstrated to provide a sensitivity improvement in HP- ^{13}C MR spectroscopic data by an order of magnitude and a moderate SNR gain for image data.^{38,39} The relative mean SNR values from the noise-added and denoised lactate signals ($Rel. \overline{SNR}_{Lac}$), plotted in Figure 2B, demonstrate that GL-HOSVD outperforms TRI in terms of the SNR enhancement, which was almost 3 times greater than that of TRI, providing an overall a >8-fold SNR increase with respect to the noise-added images. Similar SNR enhancements were observed from the denoised pyruvate signals as well as at different noise levels. Figure 2C depicts mean SSIM values calculated from the 500 simulated lactate images. The more similar the denoised and noise-free images are, the closer the SSIM is to 1. The GL-HOSVD images are close to 1 at all time points, consistently higher than those from the TRI images. As the signals diminish due to T_1 relaxation and RF utilization, the SSIM values deviate from unity more rapidly with TRI than GL-HOSVD. These observations indicate that GL-HOSVD better preserves image details than TRI, especially in low-SNR images.

3.1.2 Accuracy of k_{pL} quantification—Evaluating the effect of denoising on the voxel-wise quantification of metabolic conversion enabled a further comparison of GL-HOSVD versus TRI approaches. Figure 3 shows examples of estimated k_{pL} maps from the simulated pyruvate and lactate images with increasing amounts of noise. The left and right image sets are from a central and superior slice of the brain phantom. The reference k_{pL} map for each slice is shown on the top. The image set below displays the k_{pL} maps from the non-denoised images and the corresponding GL-HOSVD and TRI images in the presence of Gaussian noise of $\sigma_n = 0.2, 0.3,$ and 0.4 . Comparisons between the k_{pL} maps from the GL-HOSVD images (second column) and those from the TRI images (third column) show the superior performance of GL-HOSVD in recovering the reference k_{pL} information relative to TRI, especially in the white matter that was simulated with a lower k_{pL} than the gray matter. The k_{pL} values from the GL-HOSVD images were found to be more uniform within a compartment, while those from the TRI images had greater variability. This can

be clearly seen from the uniformity of white matter in the superior slice processed with GL-HOSVD (Figure 3b,e,h). From 500 replicate simulations, the mean of voxel-by-voxel k_{pL} errors (i.e. bias) was evaluated as displayed in Figure 4. Overall, smaller k_{pL} errors were obtained from GL-HOSVD, and they showed 20% reduction compared to TRI on average. Also, the errors were relatively greater from the white matter versus gray matter as expected from the lower k_{pL} value of white matter. The plot of mean k_{pL} errors from the white and gray matter at different noise levels against the original SNR_{auc} of lactate showed that when $SNR_{auc} < 3$, the k_{pL} error from GL-HOSVD becomes higher than 20% (Figure S2). Elevated k_{pL} errors from GL-HOSVD were also observed at the boundary of the gray and white matter compartments at the highest noise levels, as a result of the binary gray and white matter masks used for the simulation. These errors indicated that the k_{pL} values from GL-HOSVD from the voxels at the boundary between the gray and white matter were mostly overestimated while those from voxels at the boundary between the gray matter and background were underestimated. Overall, the mean k_{pL} value decreased by 2 – 3 % at the highest noise level simulated. The k_{pL} precision displayed in Figure 5 shows that k_{pL} values from the GL-HOSVD data were more precise. On average, the mean standard errors from GL-HOSVD were 3 times smaller than those from TRI. Compared to the non-denoised data, k_{pL} quantification was approximately 9 – 10 times more precise with the GL-HOSVD data. This improvement in k_{pL} precision translated into an increase in the number of reliable voxels comprising kinetic rate maps, after application of SNR threshold and k_{pL} fitting error criteria. The k_{pL} error and precision maps for the superior slice of the brain phantom are displayed in Figure S1. Similar to the k_{pL} accuracy, the accuracy of lactate-to-pyruvate ratio from temporally summed metabolite signals (AUC ratio) was also improved by 20% compared to TRI (Figure S3).

3.2. Denoising results for in-vivo data using GL-HOSVD

3.2.1 Sensitivity improvement—Application of GL-HOSVD to dynamic HP-¹³C EPI scans of six healthy human brain volunteers demonstrated the practical performance of this method. Figure 6A displays the original non-denoised and denoised pyruvate, lactate, and bicarbonate images from one volunteer dataset. The original metabolite images, shown in the first row for each metabolite, were observed with the peak dynamic SNR of 569, 25, and 6.5 for pyruvate, lactate, and bicarbonate, respectively. Background noise was successfully reduced by applying the GL-HOSVD method, yielding the denoised images in the second row for each metabolite. The most substantial improvement in image quality was observed for the bicarbonate images. The bicarbonate signals were barely distinguishable from the noise of the original images, especially at later time points, but were readily observable (apparent SNR > 10) after denoising. For lactate, the edges were better defined in the denoised images than the original data. Also, spatially and temporally different lactate distribution remained preserved in the denoised images without noticeable distortion which can be caused by the dynamics of high SNR signals. High similarity between the denoised and original pyruvate images suggests minimal bias and corruption of the originally high-SNR resonances. In Figure 6B, the sensitivity improvement in the denoised metabolite images throughout the entire course of the acquisition is illustrated with mean SNR relative to the maximum value from the original data. The apparent SNR gain for the first 10

timeframes was determined as 5.4 ± 0.3 , 4.8 ± 0.2 , and 5.8 ± 1.6 for pyruvate, lactate, and bicarbonate, respectively.

In Figure 7, pre- and post-denoised pyruvate, lactate, and bicarbonate images from 5 central slices of another healthy volunteer (HV-02) are shown. These images represent the signals at the early and late time points, obtained 14 and 38 s after the saline flush following the pyruvate injection. The late time scans demonstrate well the sensitivity enhancement in the denoised images of all three metabolite signals. In particular, the brain became more clearly defined in the denoised bicarbonate images than the original data, where the signal intensities were on the same order of magnitude as the noise. The multi-slice images from the first volunteer data (HV-01; Figure 6) are presented in Supporting Information (Figure S4). Figure 8 displays the denoising of the volunteer dataset acquired using a volume coil (HV-06) and illustrates the performance of GL-HOSVD at higher noise levels. This dataset exhibited the lowest SNR among the 6 datasets analyzed in this study (see Table S1) due to the reduced sensitivity of the single channel birdcage coil. The denoised images demonstrated significantly improved sensitivity for all metabolites, although the denoised bicarbonate images showed potentially limited reliability for this denoising method at exceptionally low SNR. Examples of the original and denoised dynamic data of the metabolites from a single voxel are shown for each of three volunteer datasets in Figure S5. This figure shows that the late-time, low-intensity pyruvate signals can be well preserved after denoising although the pyruvate signal intensities at later timepoints are 5–10 times smaller than the peak intensity. Also, the denoised bicarbonate traces follow the original traces well despite high noise at the initial timeframes.

3.2.2 Quantitative analysis—The improvement of fit quality in kinetic analysis and spatial coverage for the k_{pL} and k_{pB} maps using GL-HOSVD was verified on in vivo datasets from the healthy volunteers. The SNR and error criteria were applied to generate these maps as described in Methods 2.3.2. Figure 9 shows representative k_{pL} and k_{pB} values overlaid on the anatomical images and their distributions. The brain coverage of k_{pL} maps from the GL-HOSVD data (bottom row, Figure 9A) was improved from 69 to 94%. There was no noticeable difference in the image contrast between the original and denoised maps, which can be also seen from similar k_{pL} distributions in both the original and GL-HOSVD data. This was supported by good voxel-by-voxel agreement of k_{pL} values between the original and denoised maps (Figure S6A). A larger impact on the spatial coverage was observed from the k_{pB} maps following denoising, with nearly a 3-fold increase from 12 to 37% (Figure 9B). The k_{pB} distributions illustrated that newly estimated k_{pB} values from the denoised data were mostly lower than the average value of k_{pB} from the original data. Voxel-by-voxel comparison between the original and denoised k_{pB} values showed slightly decreased values of the denoised data to $85 \pm 6\%$ of the original data on average (Figure S6B), similar to the bias observed in numerical simulations of high noise. As a result, the average k_{pB} value from the denoised data was decreased by 1.6 times as compared to that of the original data. Figure 9C shows the kinetic fits of the denoised and original traces of bicarbonate signals from the selected voxels indicated by white arrows. The noise removal enabled k_{pB} quantification from the left voxel, which would otherwise be neglected from the k_{pB} mapping because of poor fit quality and unsatisfied error criteria. From the

second voxel on the right, the k_{PB} precision was improved by 2 times in the denoised data, with less than 15 % of the relative standard error. Additionally, k_{PL} fits from four selected voxels with varying lactate SNR ($SNR_{auc} = 2.4\sim 17$) were compared (Figure S7). Here, we included a voxel with $SNR_{auc} < 3$ for raw lactate signal (SNR criteria for kinetic analysis) to show the data and fit quality. From the voxels with lactate SNR of 14 and 17, the fitted k_{PL} values from the original and denoised data showed good agreement while the k_{PL} precision was much higher with the denoised data. With lower lactate SNR, the k_{PL} values estimated from the original data were not reliably calculated due to the elevated noise floor, in agreement with numerical simulations. The relative standard k_{PL} error was 42% from the voxel with SNR_{auc} of 2.4, which improved to 6% after denoising. Table S1 summarizes the improvement in SNR_{auc} and spatial coverage of k_{PL} and k_{PB} maps, and the mean voxel-wise k_{PL} and k_{PB} values from the evaluated brain volume from the six healthy volunteers.

4. Discussion

In this study, we implemented and tested the patch-based denoising method of GL-HOSVD in the processing pipeline for dynamic HP-¹³C MR images of the human brain. The performance of this method for improving SNR and the accuracy of quantified kinetic rates was first evaluated with numerical simulations, where GL-HOSVD denoising was shown to be superior to TRI. GL-HOSVD denoising was then applied to HP-¹³C EPI datasets from healthy brain volunteers, where it improved the detection of bicarbonate and enhanced quantification of k_{PL} and k_{PB} using a 32- or 24-channel array (Figures 6,7, and 9) and a single-channel volume coil (Figure 8) that is used for studies at multiple sites.²⁶

Simulation studies showed increased k_{PL} error in the GL-HOSVD denoised data at the boundary between the white and gray matter regions of the brain phantom which manifested as blurring of the periphery of white matter in k_{PL} maps. The sharp signal discontinuity at the interface between the white and gray matter of the metabolic phantom likely contributed to these high k_{PL} errors. A smaller patch size can alleviate this problem but comes at the cost of less effective noise reduction (Figure S8); nevertheless, this artifact would be less apparent for human studies due to the realistic EPI PSF and blurring related to T_2^* decay and B_0 inhomogeneity.

The matrix size of the simulated data was twice as large as the healthy human carbon-13 data for in-plane dimensions with a two-fold finer spatial resolution. This was to represent detailed features like gray/white matter contrast in the simulated brain phantom for testing the denoising performance. No adjustments were needed to the GL-HOSVD parameters determined from the simulation such as k_{local} , k_{global} , patch size, and step size when denoising the low-resolution human data. Similar to aforementioned effects of patch size, the smoothing artifacts were reduced by lowering k_{local} and k_{global} parameters, but at the expense of SNR gain. A variation in step size and size of the search window made no appreciable change in the outputs from the simulation. The denoising parameters may need to be optimized for other data types such as of different organs or spatial resolution using relevant numerical phantoms.

In our study, we expressed the 5D dynamic multi-slice, multi-frequency HP-¹³C EPI dataset as a 3D tensor per each frequency and slice, and denoised each metabolite on a slice-by-slice basis. With this approach, no crosstalk between different metabolites can occur. When performing the GL-HOSVD denoising on the whole 4D metabolite dataset, a slight increase in the apparent SNR was observed from simulations. However, crosstalk between different slices was apparent in the denoised images (data not shown). This was likely due to the small number of slices (8) in the z-dimension and may be obviated by acquiring more slices or using a smaller patch size in that dimension.

As described in Figure S2, the simulation results indicated that the accuracy of kinetic rate quantification from the GL-HOSVD denoised images depends on the SNR_{auc} of lactate in the raw data. These results can be interpreted in terms of minimum SNR needed to accurately quantify metabolism rather than just being relevant for the pyruvate-to-lactate conversion. For instance, while the simulations did not explicitly include bicarbonate, it would have similar dynamics modeled by the same two-site unidirectional kinetic model, and the SNR_{auc} can be used to help guide interpretation and analysis of denoised data for both k_{pL} and k_{pB} . Based on the simulations, kinetic rates can be estimated with less than 20% error from any voxels with SNR_{auc} of 3 or higher. While kinetic rates can still be estimated at lower SNR, care must be taken when interpreting this data due to the potential for increased bias. These simulations also did not include other potential confounders, such as recirculation or motion. However, the in-vivo datasets suggested that the timecourse of pyruvate recirculation can be preserved after denoising (Figure S5).

More than fivefold improvement in SNR following denoising of the volunteer datasets, indicates the possibility of acquiring metabolic data at higher spatial resolution in future clinical studies, thereby mitigating partial volume effects and facilitating extraction of metabolic information for improved clinical management. It could be particularly beneficial for other image-based ¹³C studies using HP [2-¹³C]pyruvate, [¹³C]urea and [1-¹³C]α-ketoglutarate, exhibiting lower SNR compared to [1-¹³C]pyruvate due to shorter T_1 or lower polarization.

5. Conclusion

A patch-based approach for denoising images was investigated and applied in human HP-¹³C brain studies to enhance the sensitivity of metabolite signals from HP [1-¹³C]pyruvate MRI data. With sensitivity enhancements of 5+ fold, low SNR metabolites were better visualized, and k_{pL} and k_{pB} maps with greater brain coverage were obtained, especially when using a volume head coil. This demonstrated the benefit of patch-based denoising to improve the quality of HP-¹³C images and spatial resolution for future studies.

Supplementary Material

Refer to Web version on PubMed Central for supplementary material.

Acknowledgements

This research was supported by NIH (P41EB013598, P01CA118816, T32CA151022, P50CA097257) and the UCSF NICO project.

Reference

1. Ardenkjær-Larsen JH, Fridlund B, Gram A, et al. Increase in signal-to-noise ratio of > 10,000 times in liquid-state NMR. *PNAS*. 2003;100(18):10158–10163. doi:10.1073/pnas.1733835100 [PubMed: 12930897]
2. Wang ZJ, Ohliger MA, Larson PEZ, et al. Hyperpolarized ^{13}C MRI: State of the Art and Future Directions. *Radiology*. 2019;291(2):273–284. doi:10.1148/radiol.2019182391 [PubMed: 30835184]
3. Kurhanewicz J, Vigneron DB, Ardenkjaer-Larsen JH, et al. Hyperpolarized ^{13}C MRI: Path to Clinical Translation in Oncology. *Neoplasia*. 2019;21(1):1–16. doi:10.1016/j.neo.2018.09.006 [PubMed: 30472500]
4. Park I, Larson PEZ, Zierhut ML, et al. Hyperpolarized ^{13}C magnetic resonance metabolic imaging: application to brain tumors. *Neuro-Oncology*. 2010;12(2):133–144. doi:10.1093/neuonc/nop043 [PubMed: 20150380]
5. Park JM, Josan S, Grafendorfer T, et al. Measuring mitochondrial metabolism in rat brain in vivo using MR Spectroscopy of hyperpolarized $[2-^{13}\text{C}]$ pyruvate: MEASURING MITOCHONDRIAL METABOLISM IN BRAIN USING $[2-^{13}\text{C}]$ PYRUVATE. *NMR Biomed*. 2013;26(10):1197–1203. doi:10.1002/nbm.2935 [PubMed: 23553852]
6. Mishkovsky M, Anderson B, Karlsson M, et al. Measuring glucose cerebral metabolism in the healthy mouse using hyperpolarized ^{13}C magnetic resonance. *Sci Rep*. 2017;7(1):11719. doi:10.1038/s41598-017-12086-z [PubMed: 28916775]
7. Mishkovsky M, Comment A, Gruetter R. *In Vivo* Detection of Brain Krebs Cycle Intermediate by Hyperpolarized Magnetic Resonance. *J Cereb Blood Flow Metab*. 2012;32(12):2108–2113. doi:10.1038/jcbfm.2012.136 [PubMed: 22990416]
8. Najac C, Ronen SM. MR Molecular Imaging of Brain Cancer Metabolism Using Hyperpolarized ^{13}C Magnetic Resonance Spectroscopy. *Topics in Magnetic Resonance Imaging*. 2016;25(5):187–196. doi:10.1097/RMR.000000000000104 [PubMed: 27748711]
9. Park I, Larson PEZ, Gordon JW, et al. Development of methods and feasibility of using hyperpolarized carbon-13 imaging data for evaluating brain metabolism in patient studies: Hyperpolarized Carbon-13 Metabolic Imaging of Patients With Brain Tumors. *Magn Reson Med*. 2018;80(3):864–873. doi:10.1002/mrm.27077 [PubMed: 29322616]
10. Chung BT, Chen H-Y, Gordon J, et al. First hyperpolarized $[2-^{13}\text{C}]$ pyruvate MR studies of human brain metabolism. *Journal of Magnetic Resonance*. 2019;309:106617. doi:10.1016/j.jmr.2019.106617 [PubMed: 31648132]
11. Hsu PP, Sabatini DM. Cancer Cell Metabolism: Warburg and Beyond. *Cell*. 2008;134(5):703–707. doi:10.1016/j.cell.2008.08.021 [PubMed: 18775299]
12. Ward PS, Thompson CB. Metabolic Reprogramming: A Cancer Hallmark Even Warburg Did Not Anticipate. *Cancer Cell*. 2012;21(3):297–308. doi:10.1016/j.ccr.2012.02.014 [PubMed: 22439925]
13. Crane JC, Gordon JW, Chen H-Y, et al. Hyperpolarized ^{13}C MRI data acquisition and analysis in prostate and brain at University of California, San Francisco. *NMR in Biomedicine*. Published online March 19, 2020:e4280. doi:10.1002/nbm.4280 [PubMed: 32189442]
14. Park I, Larson PEZ, Gordon JW, et al. Development of Methods and Feasibility of Using Hyperpolarized Carbon-13 Imaging Data for Evaluating Brain Metabolism in Patient Studies. *Magnetic Resonance in Medicine*. 2018;(80):864–873. doi:10.1002/mrm.27077 [PubMed: 29322616]
15. Miloushev VZ, Granlund KL, Boltyanskiy R, et al. Metabolic Imaging of the Human Brain with Hyperpolarized ^{13}C Pyruvate Demonstrates ^{13}C Lactate Production in Brain Tumor Patients. *Cancer Res*. 2018;78(14):3755–3760. doi:10.1158/0008-5472.CAN-18-0221 [PubMed: 29769199]

16. Autry AW, Gordon JW, Chen H-Y, et al. Characterization of serial hyperpolarized ^{13}C metabolic imaging in patients with glioma. *NeuroImage: Clinical*. 2020;27:102323. doi:10.1016/j.nicl.2020.102323 [PubMed: 32623139]
17. Lee CY, Soliman H, Geraghty BJ, et al. Lactate topography of the human brain using hyperpolarized ^{13}C -MRI. *NeuroImage*. 2020;204:116202. doi:10.1016/j.neuroimage.2019.116202 [PubMed: 31557546]
18. Grist JT, McLean MA, Riemer F, et al. Quantifying normal human brain metabolism using hyperpolarized $[1-^{13}\text{C}]$ pyruvate and magnetic resonance imaging. *NeuroImage*. 2019;189:171–179. doi:10.1016/j.neuroimage.2019.01.027 [PubMed: 30639333]
19. Gordon JW, Hansen RB, Shin PJ, Feng Y, Vigneron DB, Larson PEZ. 3D hyperpolarized C-13 EPI with calibrationless parallel imaging. *Journal of Magnetic Resonance*. 2018;289:92–99. doi:10.1016/j.jmr.2018.02.011 [PubMed: 29476930]
20. Tang S, Bok R, Qin H, et al. A metabolite-specific 3D stack-of-spiral bSSFP sequence for improved lactate imaging in hyperpolarized $[1-^{13}\text{C}]$ pyruvate studies on a 3T clinical scanner. *Magn Reson Med*. 2020;84(3):1113–1125. doi:10.1002/mrm.28204 [PubMed: 32086845]
21. Deh K, Granlund KL, Eskandari R, Kim N, Mamakhanyan A, Keshari KR. Dynamic volumetric hyperpolarized ^{13}C imaging with multi-echo EPI. *Magn Reson Med*. Published online August 15, 2020:mrm.28466. doi:10.1002/mrm.28466
22. Chen H, Larson PEZ, Gordon JW, et al. Technique development of 3D dynamic CS-EPSI for hyperpolarized ^{13}C pyruvate MR molecular imaging of human prostate cancer. *Magn Reson Med*. 2018;80(5):2062–2072. doi:10.1002/mrm.27179 [PubMed: 29575178]
23. Larson PEZ, Kerr AB, Chen AP, et al. Multiband excitation pulses for hyperpolarized ^{13}C dynamic chemical-shift imaging. *Journal of Magnetic Resonance*. 2008;194(1):121–127. doi:10.1016/j.jmr.2008.06.010 [PubMed: 18619875]
24. Gordon JW, Autry AW, Tang S, et al. A variable resolution approach for improved acquisition of hyperpolarized ^{13}C metabolic MRI. *Magn Reson Med*. 2020;84(6):2943–2952. doi:10.1002/mrm.28421 [PubMed: 32697867]
25. Autry AW, Gordon JW, Carvajal L, et al. Comparison between 8- and 32-channel phased-array receive coils for in vivo hyperpolarized ^{13}C imaging of the human brain. *Magn Reson Med*. 2019;82(2):833–841. doi:10.1002/mrm.27743 [PubMed: 30927300]
26. Sánchez-Heredia JD, Olin RB, McLean MA, et al. Multi-site benchmarking of clinical ^{13}C RF coils at 3T. *Journal of Magnetic Resonance*. 2020;318:106798. doi:10.1016/j.jmr.2020.106798 [PubMed: 32755748]
27. Manjon J, Carbonellcaballero J, Lull J, Garciamarti G, Martibonmati L, Robles M. MRI denoising using Non-Local Means. *Medical Image Analysis*. 2008;12(4):514–523. doi:10.1016/j.media.2008.02.004 [PubMed: 18381247]
28. Meurée C, Maurel P, Ferré J-C, Barillot C. Patch-based super-resolution of arterial spin labeling magnetic resonance images. *NeuroImage*. 2019;189:85–94. doi:10.1016/j.neuroimage.2019.01.004 [PubMed: 30633964]
29. Maggioni M, Katkovnik V, Egiazarian K, Foi A. Nonlocal Transform-Domain Filter for Volumetric Data Denoising and Reconstruction. *IEEE Trans on Image Process*. 2013;22(1):119–133. doi:10.1109/TIP.2012.2210725
30. Wood JC, Johnson KM. Wavelet Packet Denoising of Magnetic Resonance Images:Importance of Rician Noise at Low SNR. *Magnetic Resonance in Medicine*. 1999;41:631–635. [PubMed: 10204890]
31. Ma C, Clifford B, Liu Y, et al. High-resolution dynamic ^{31}P -MRSI using a low-rank tensor model: ^{31}P -Spice. *Magn Reson Med*. 2017;78(2):419–428. doi:10.1002/mrm.26762 [PubMed: 28556373]
32. Liu Y, Ma C, Clifford B, Lam F, Johnson C, Liang Z-P. Improved Low-Rank Filtering of Magnetic Resonance Spectroscopic Imaging Data Corrupted by Noise and B_0 Field Inhomogeneity. *IEEE Trans Biomed Eng*. Published online 2015:1–1. doi:10.1109/TBME.2015.2476499
33. Nguyen HM, Peng X, Do MN, Liang Z-P. Denoising MR Spectroscopic Imaging Data With Low-Rank Approximations. *IEEE Trans Biomed Eng*. 2013;60(1):78–89. doi:10.1109/TBME.2012.2223466 [PubMed: 23070291]

34. Zhang X, Peng J, Xu M, et al. Denoise diffusion-weighted images using higher-order singular value decomposition. *NeuroImage*. 2017;156:128–145. doi:10.1016/j.neuroimage.2017.04.017 [PubMed: 28416450]
35. Zhang X, Xu Z, Jia N, et al. Denoising of 3D magnetic resonance images by using higher-order singular value decomposition. *Medical Image Analysis*. 2015;19(1):75–86. doi:10.1016/j.media.2014.08.004 [PubMed: 25291148]
36. De Lathauwer L, De Moor B, Vandewalle J. A Multilinear Singular Value Decomposition. *SIAM J Matrix Anal & Appl*. 2000;21(4):1253–1278. doi:10.1137/S0895479896305696
37. Rajwade A, Rangarajan A, Banerjee A. Image Denoising Using the Higher Order Singular Value Decomposition. *IEEE Trans Pattern Anal Mach Intell*. 2013;35(4):849–862. doi:10.1109/TPAMI.2012.140 [PubMed: 22732660]
38. Brender JR, Kishimoto S, Merkle H, et al. Dynamic Imaging of Glucose and Lactate Metabolism by ^{13}C -MRS without Hyperpolarization. *Sci Rep*. 2019;9(1):3410. doi:10.1038/s41598-019-38981-1 [PubMed: 30833588]
39. Chen H, Autry AW, Brender JR, et al. Tensor image enhancement and optimal multichannel receiver combination analyses for human hyperpolarized ^{13}C MRSI. *Magn Reson Med*. 2020;84(6):3351–3365. doi:10.1002/mrm.28328 [PubMed: 32501614]
40. Donoho DL, Johnstone IM. Ideal spatial adaptation by wavelet shrinkage. *Biometrika*. 1994;81(3):425–455. doi:10.1093/biomet/81.3.425
41. Collins DL, Zijdenbos AP, Kollokian V, et al. Design and construction of a realistic digital brain phantom. *IEEE Trans Med Imaging*. 1998;17(3):463–468. doi:10.1109/42.712135 [PubMed: 9735909]
42. Larson PEZ, Chen H-Y, Gordon JW, et al. Investigation of analysis methods for hyperpolarized ^{13}C -pyruvate metabolic MRI in prostate cancer patients: Hyperpolarized Pyruvate Prostate Cancer Analysis Methods. *NMR in Biomedicine*. 2018;31(11):e3997. doi:10.1002/nbm.3997 [PubMed: 30230646]
43. Mammoli D, Carvajal L, Slater JB, et al. Kinetic Modeling of Hyperpolarized Carbon-13 Pyruvate Metabolism in the Human Brain. *IEEE Trans Med Imaging*. 2020;39(2):320–327. doi:10.1109/TMI.2019.2926437 [PubMed: 31283497]
44. Wang Z, Bovik AC, Sheikh HR, Simoncelli EP. Image Quality Assessment: From Error Visibility to Structural Similarity. *IEEE Trans on Image Process*. 2004;13(4):600–612. doi:10.1109/TIP.2003.819861
45. Gordon JW, Chen H, Autry A, et al. Translation of Carbon-13 EPI for hyperpolarized MR molecular imaging of prostate and brain cancer patients. *Magn Reson Med*. 2019;81(4):2702–2709. doi:10.1002/mrm.27549 [PubMed: 30375043]
46. Zhu Z, Zhu X, Ohliger MA, et al. Coil combination methods for multi-channel hyperpolarized ^{13}C imaging data from human studies. *Journal of Magnetic Resonance*. 2019;301:73–79. doi:10.1016/j.jmr.2019.01.015 [PubMed: 30851668]
47. Jenkinson M, Smith S. A global optimisation method for robust affine registration of brain images. *Medical Image Analysis*. 2001;5(2):143–156. doi:10.1016/S1361-8415(01)00036-6 [PubMed: 11516708]
48. Zhang Y, Brady M, Smith S. Segmentation of brain MR images through a hidden Markov random field model and the expectation-maximization algorithm. *IEEE Trans Med Imaging*. 2001;20(1):45–57. doi:10.1109/42.906424 [PubMed: 11293691]

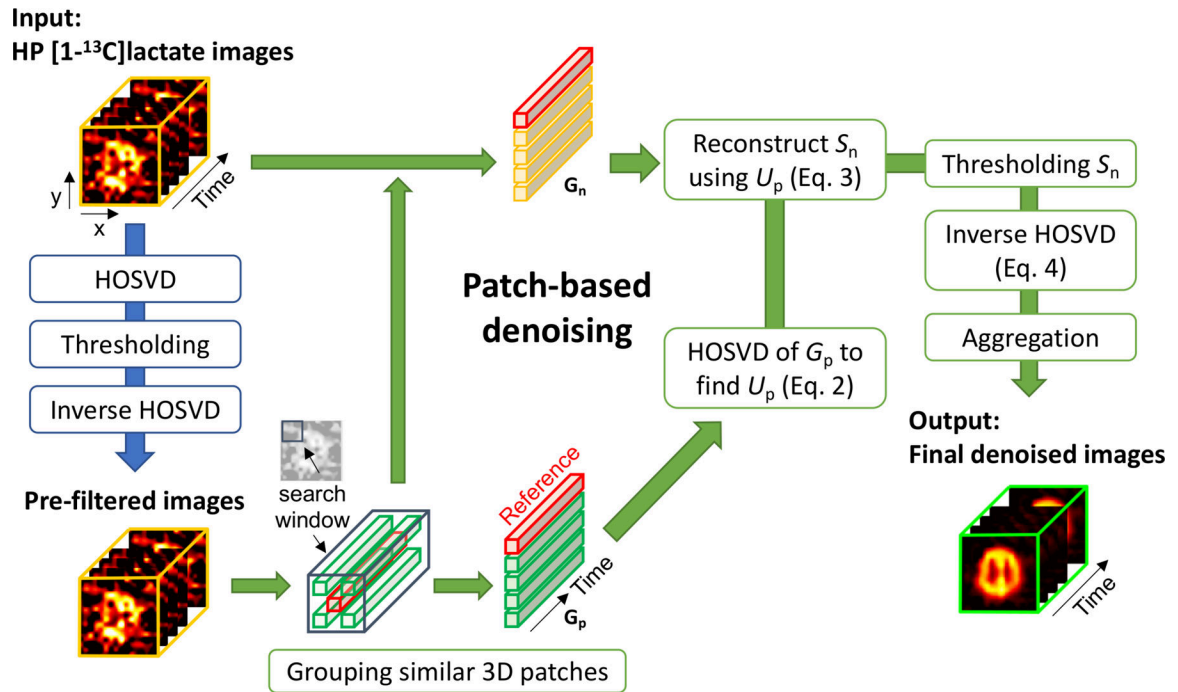


Figure 1. Diagram of the GL-HOSVD algorithm.

The GL-HOSVD algorithm includes a prefiltering stage (left vertical) followed by the patch-based denoising. From the pre-filtered images, similar patches are searched and grouped into a 4D stack, G_p . Factor matrices U_p obtained from HOSVD of G_p are utilized to reconstruct HOSVD transform coefficients of G_n (S_n). By hard thresholding S_n , the denoised stacks are estimated by inverse HOSVD, and the multiple estimates at each pixel are aggregated to obtain final denoised images. The figure was adapted for HP-¹³C MRI from Zhang et al.³⁴ including dynamic HP [1-¹³C]lactate images of a brain slice as an example. Denoising was performed on dynamic data on a slice-by-slice basis and was done separately for each metabolite to avoid signal crosstalk between metabolites.

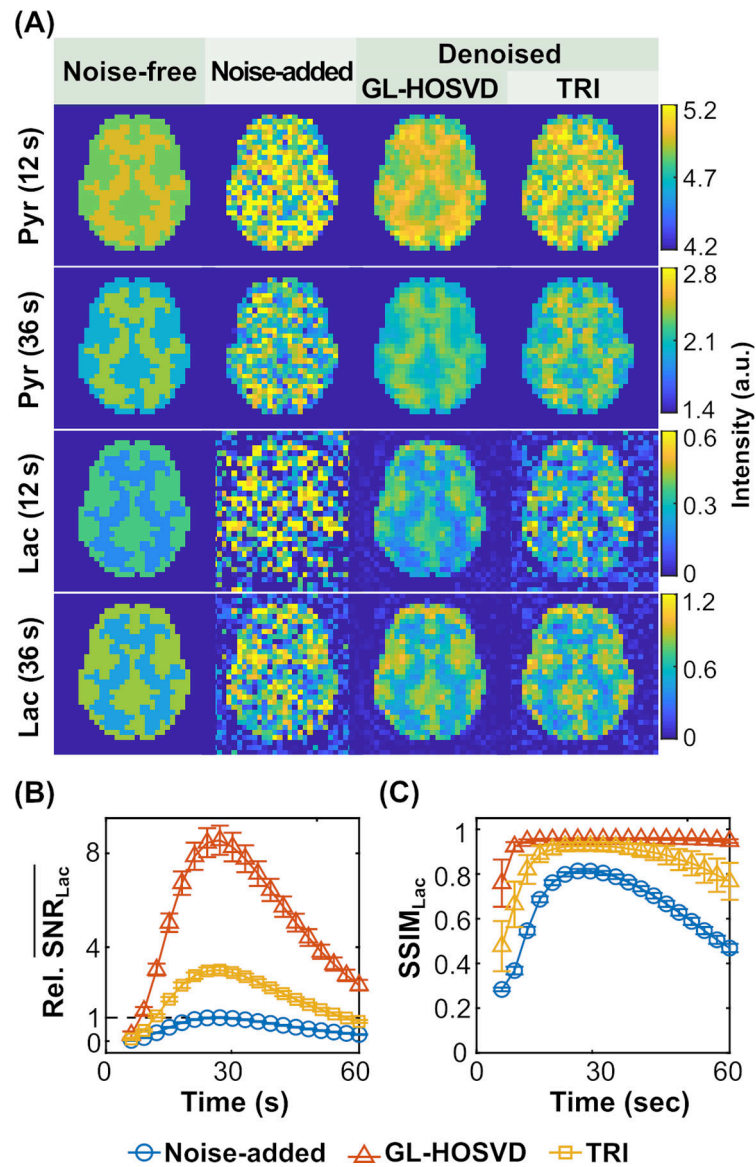


Figure 2.
Comparative Results Between the GL-HOSVD and Tensor Rank Truncation-Image Enhancement (TRI) methods for Denoising Image Data. (A) Representative images from the simulated pyruvate and lactate data with 30% Gaussian noise ($\sigma_n = 0.3$) at an early ($t=12$ s) and late ($t=36$ s) timepoint before and after denoising. In the top two rows, noise-free, noise-added, and denoised pyruvate images are displayed from left to right. The lactate images are shown in the bottom two rows; (B) Relative mean values of the signal-to-noise ratio (SNR) of the noise-added and denoised lactate signals from 500 simulated datasets. The peak \overline{SNR}_{Lac} of the noise-added data was normalized to 1. The $Rel. \overline{SNR}_{Lac}$ values showed 2–3 times higher SNR gain by using GL-HOSVD versus TRI; (C) Structural Similarity Index Metric (SSIM) values calculated for the noise-added and denoised lactate images as a function of time. The error bars indicate standard deviations from 500 simulations. High SSIM values of the GL-HOSVD images compared to the TRI

images indicate higher similarity of the denoised images to the noise-free images especially in the late scans.

Author Manuscript

Author Manuscript

Author Manuscript

Author Manuscript

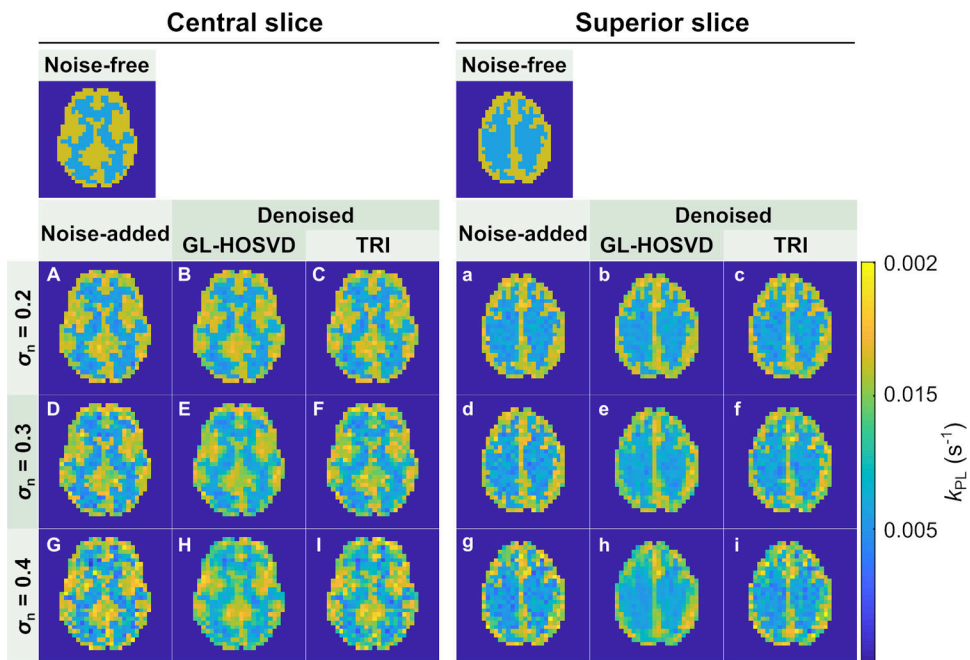


Figure 3. Simulated Estimation of Pyruvate-to-Lactate Conversion Rate (k_{PL}).

Top row: Ground-truth k_{PL} maps from a noise-free central slice (*left*) and a superior slice (*right*). The k_{PL} values of 0.015 and 0.0075 s^{-1} were assigned to the k_{PL} for gray and white matter, respectively. For the central slice, from left to right: A–C: k_{PL} maps obtained from the simulated data with the Gaussian noise of $\sigma_n = 0.2$ and those from the corresponding GL-HOSVD and TRI images; D–F: k_{PL} maps from the simulated data with the Gaussian noise of $\sigma_n = 0.3$ and G–I with $\sigma_n = 0.4$, respectively. For the superior slice, the k_{PL} maps from the noise-added and denoised data are displayed with the same order as for the central slice. The k_{PL} maps from the GL-HOSVD data showed less error than the TRI k_{PL} maps but can exhibit poor edge sharpness and over-smoothing at high noise levels.

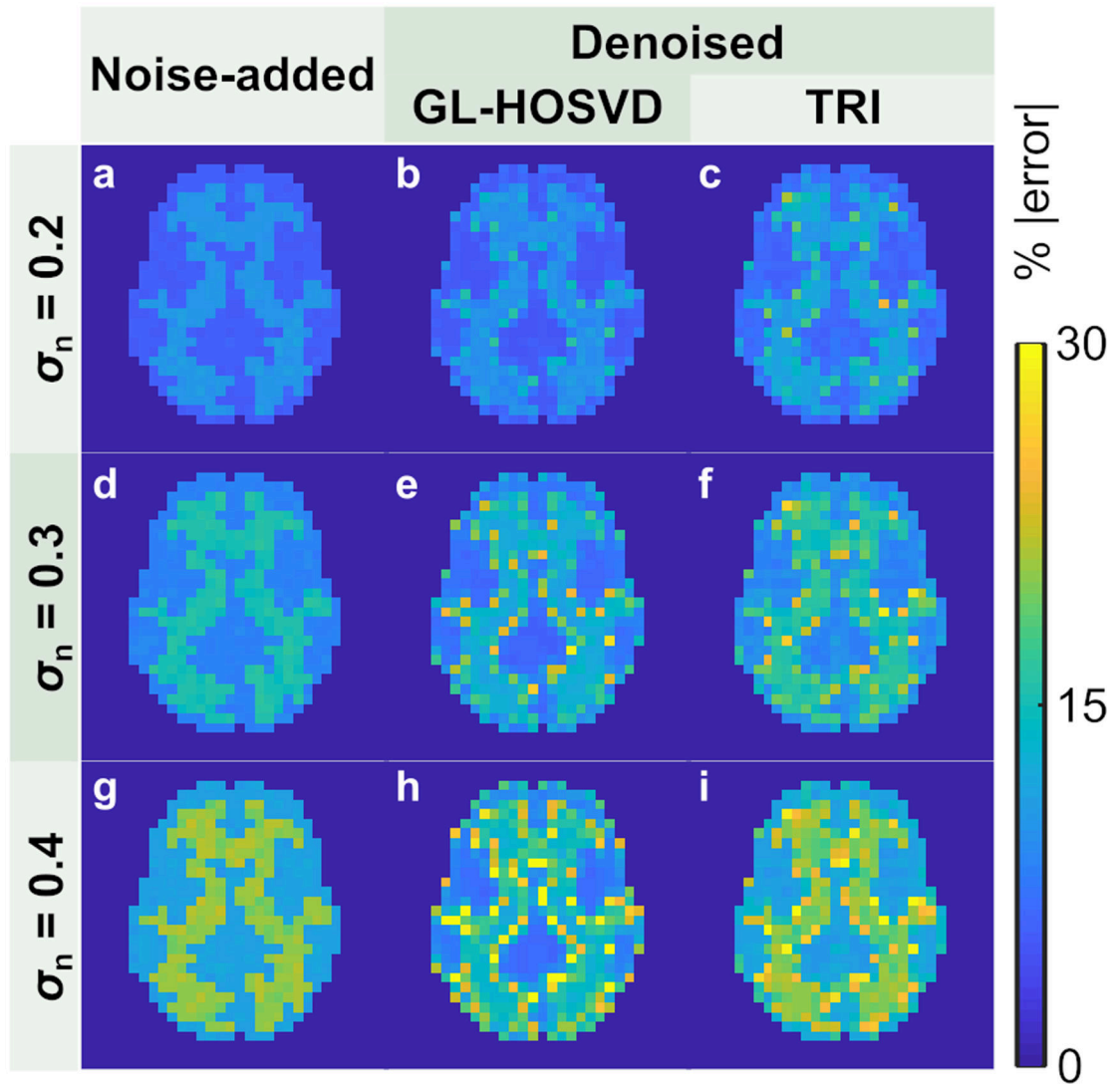
- k_{PL} accuracy

Figure 4. Simulated Assessment of k_{PL} Accuracy.

The error images showing the mean percent differences (bias) in k_{PL} estimates between noise-added and noise-free images (a,d,g); the corresponding GL-HOSVD processed and noise-free images (b,e,h); and the TRI processed and noise-free images (c,f,i), calculated from 500 simulated datasets. The standard deviation of the random Gaussian noise contained in the noise-added data is indicated on the left. Compared to the TRI data, the GL-HOSVD data show lower k_{PL} errors on average, but relatively higher errors at the boundary of the gray and white matter regions.

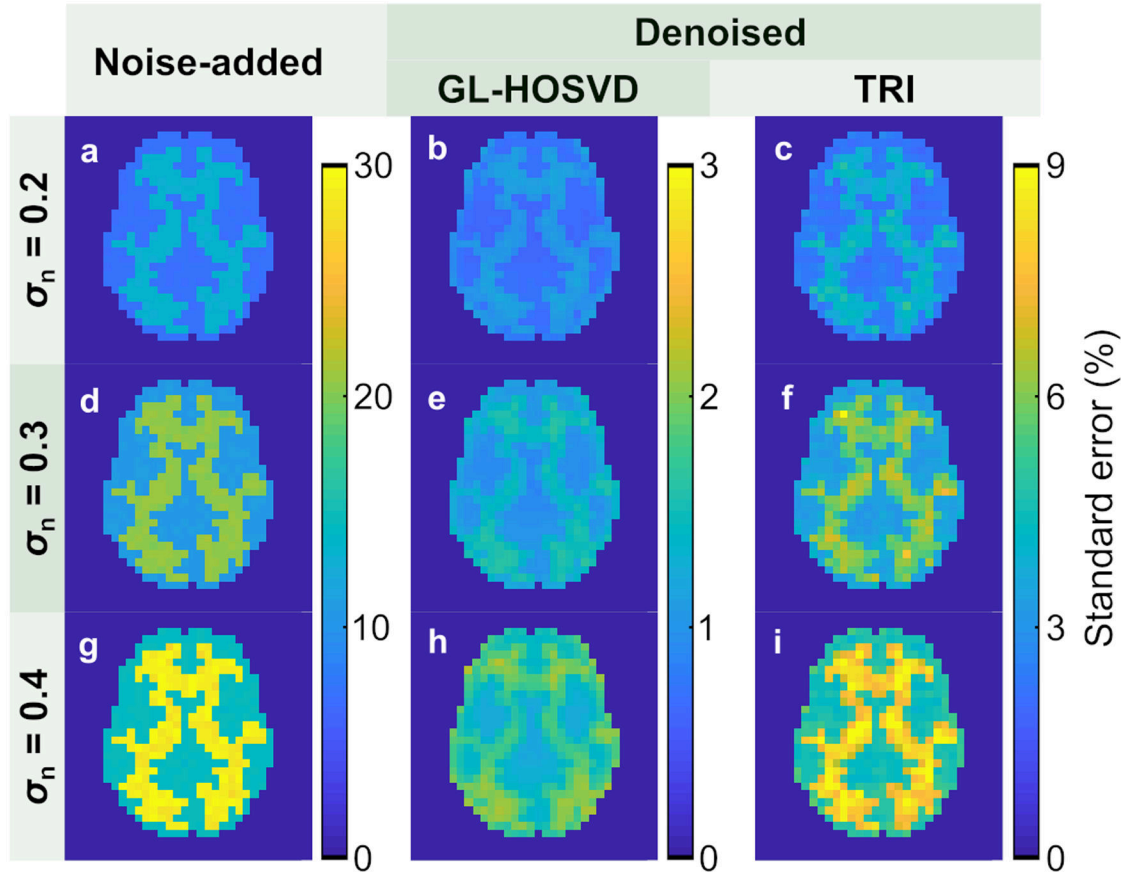
- k_{PL} precision

Figure 5. Simulated Assessment of k_{PL} Precision.

The error images showing the mean standard errors of the fitted k_{PL} values from 500 noise-added simulated data (a,d,g), and corresponding GL-HOSVD (b,e,h) and TRI images (c,f,i) at different noise levels as indicated on the left. Approximately 2 – 3 times higher k_{PL} precision was obtained from GL-HOSVD versus TRI.

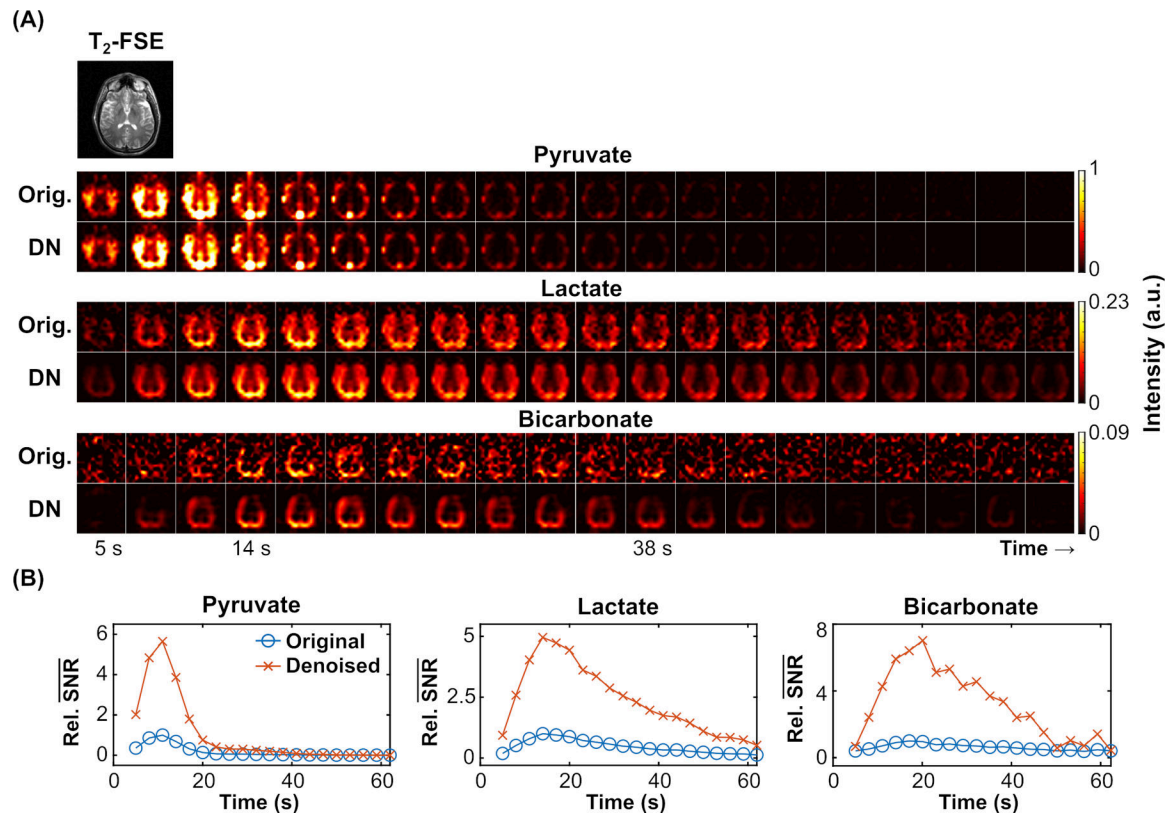


Figure 6. Dynamic Hyperpolarized Imaging of $[1-^{13}\text{C}]$ Pyruvate Metabolism.

(A) Dynamic HP- ^{13}C EPI data of $[1-^{13}\text{C}]$ pyruvate, $[1-^{13}\text{C}]$ lactate, and $[^{13}\text{C}]$ bicarbonate signals from a selected slice in a healthy brain volunteer (HV-01), acquired with the whole-brain multi-slice EPI dynamic sequence with 3 s temporal resolution. The acquisition started 5 s following the end of the saline injection at time zero. Data are shown before ('Orig.:', original) and after applying the global-local higher-order singular value decomposition ('DN': denoised). The images have been zero-filled 4-fold for display. For lactate and bicarbonate, the upper window-level was set to the overall maximum intensity voxel. For pyruvate, the upper window level was adjusted to 20% of the overall maximum intensity voxel. For anatomic reference, a ^1H T_2 -FSE (fast spin echo) image is shown on the top; (B) apparent SNR timecourse from pre- and post-denoised images of pyruvate, lactate, and bicarbonate (from left to right). Relative values of mean signal-to-noise ratio ($Rel. \overline{SNR}$) of metabolite signals from original ('o') and denoised images ('x'), displayed in (A), are plotted as a function of time with respect to the peak \overline{SNR} of the original images. The highest apparent SNR gain of 7 was observed in the denoised bicarbonate signals.

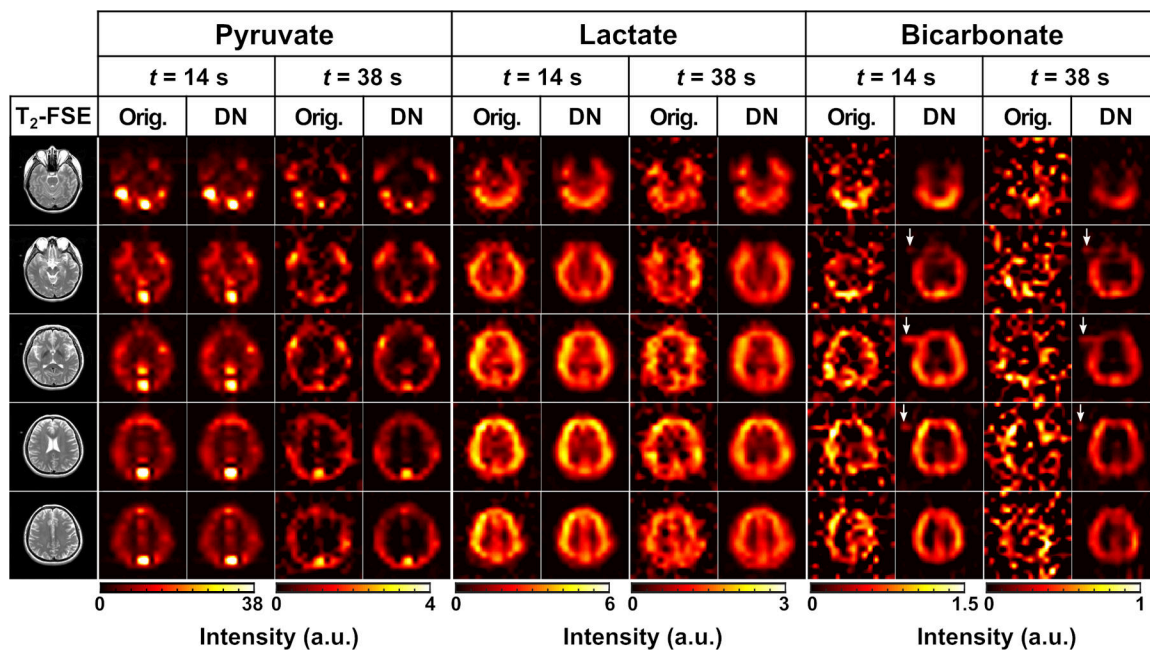


Figure 7. Denoising Results Using the GL-HOSVD for the Multi-slice, Dynamic HP-¹³C EPI Data from a Healthy Brain Volunteer.

The original (Orig.) and denoised (DN) metabolite images from an early and late timepoint ($t = 14$ and 38 s, corresponding to the 4th and 12th scans, respectively) are displayed for 5 central slices of a healthy brain volunteer (HV-02). The effect of denoising was most apparent for bicarbonate images at both timepoints; whereas the noise reduction in pyruvate and lactate images was most visible at the later time point. White arrows in the bicarbonate images indicate the signal from the [¹³C]urea phantom. For anatomic reference, ¹H T₂-FSE images are shown on the left.

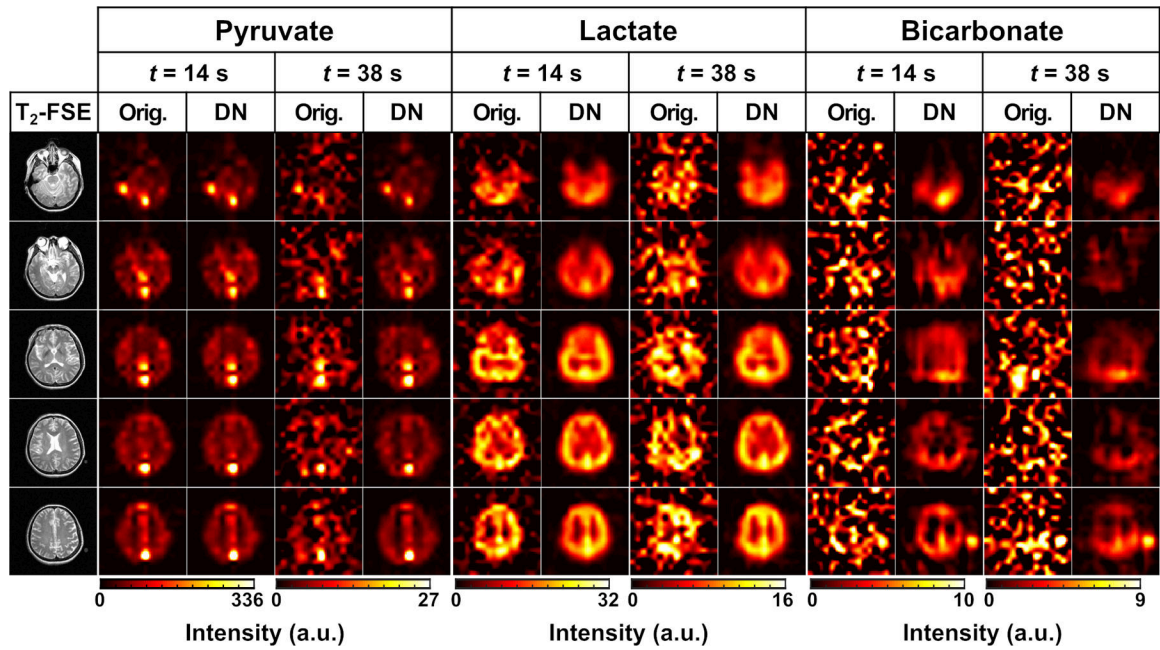


Figure 8. Denoising Results of GL-HOSVD for the Multi-slice, Dynamic HP-¹³C EPI Data Acquired from a Healthy Brain Volunteer Using a Volume Coil.

The original (Orig.) and denoised (DN) metabolite images from the early and later time points ($t = 14$ and 38 s, corresponding to the 4th and 12th scans, respectively) are displayed for 5 axial slices of a healthy brain volunteer (HV-06). The images have been zero-filled 4-fold for display. The upper window level was adjusted to 55 % (pyruvate) or 110 % (lactate and bicarbonate) of the maximum intensity voxel in the 5 slices of the denoised images. For anatomic reference, ¹H T₂-FSE images are shown on the left. Noise reduction for the pyruvate images can be clearly seen in the later time point, and at both time points for the lactate images. For bicarbonate, the denoised image quality is also greatly improved.

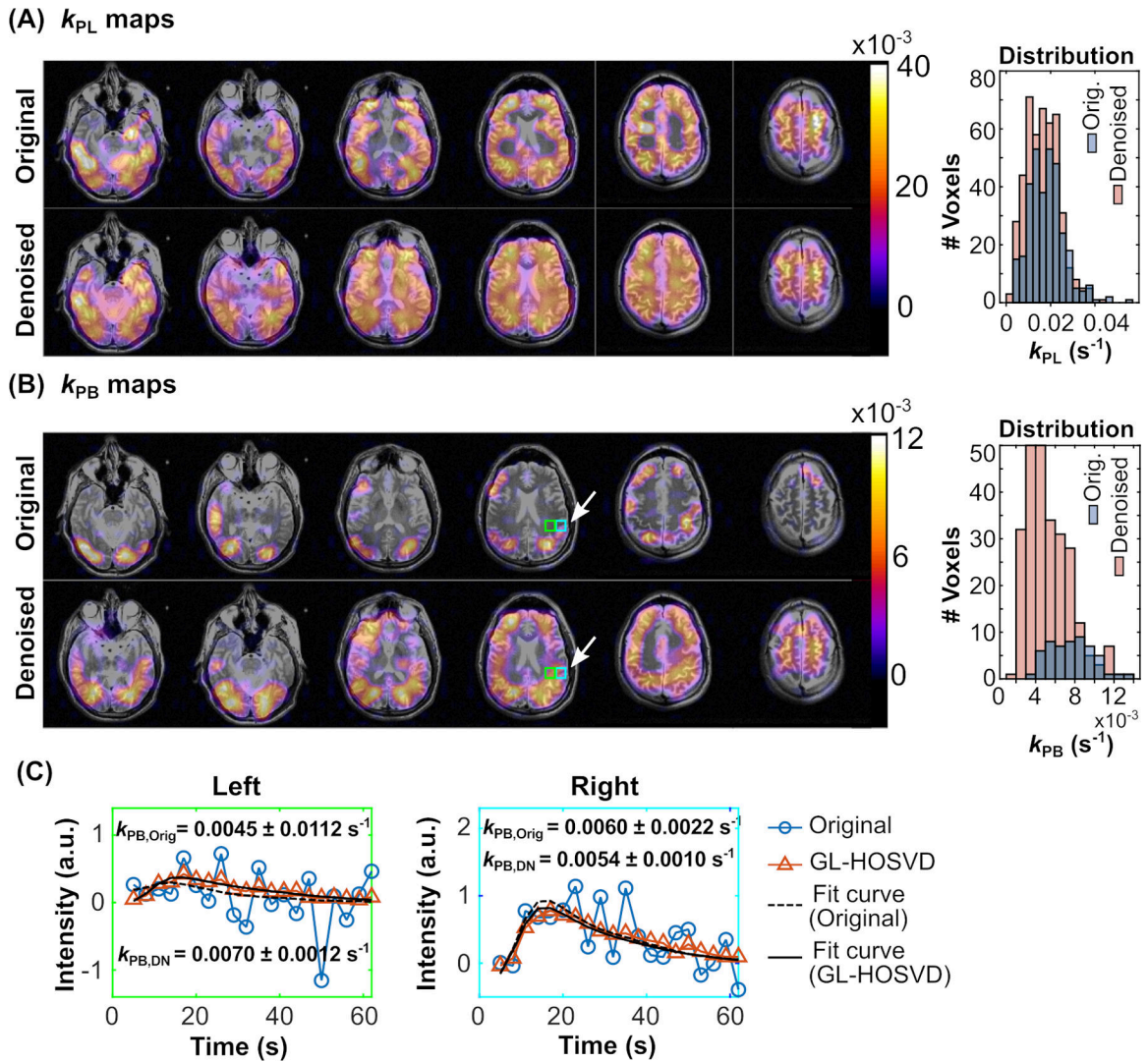


Figure 9. k_{PL} and k_{PB} Maps from a Healthy Volunteer Before and After Denoising.

(A) Left: k_{PL} maps generated from the original (top row) and the GL-HOSVD denoised (bottom row) metabolite images of a healthy volunteer (HV-01). Right: Distributions of quantified k_{PL} values from the original and denoised 32-channel images; (B) Left k_{PB} maps generated from the original data (top row) and the GL-HOSVD denoised data (bottom row). Right: Histograms of voxels with quantified k_{PB} values from the original and denoised images; both k_{PL} and k_{PB} maps have been zero-filled 4-fold for display. (C) Traces of the original and denoised bicarbonate signals in an arbitrary unit (a.u.) from 2 selected voxels, indicated by an arrow in the k_{PB} maps (B). The fitted curves from the denoised and the original data are displayed, and the corresponding k_{PB} values are denoted in the plots ($k_{PB,Orig}$: k_{PB} from the original data, $k_{PB,DN}$: k_{PB} from the denoised data). The denoised images show improved spatial coverage of k_{PL} and k_{PB} maps, particularly for white matter. For k_{PB} , the spatial coverage with acceptable fit quality is increased threefold after denoising.